The dependence of soot particle ice nucleation ability on its volatile content

Kunfeng Gao,[a,b,c] Hans-Christian Koch,[d] Chong-Wen Zhou*[a] and Zamin A. Kanji*[c]

[a.] *School of Energy and Power Engineering, Beihang University, Beijing, China.*

[b.] *Shenyuan Honours College of Beihang University, Beihang University, Beijing, China.*

[c.] *Department of Environmental Systems Science, Institute for Atmospheric and Climate Science, ETH Zurich, 8092 Zurich, Switzerland.*

[d.] *Bruker Switzerland AG, 8117 Fallanden, Switzerland*

***Correspondence:** zamin.kanji@env.ethz.ch and cwzhou@buaa.edu.cn

S1 *AF* curves for size selected ammonium nitrate and soot particles derived from different OPC channels

This section presents the Horizontal Ice Nucleation Chamber (HINC) calibration results with 200 nm ammonium nitrate particles and the ice nucleation (IN) activated fraction (*AF*) results of size selected soot particles detected in all OPC size bins (1.0, 2.0, 3.0, 4.0, 5.0 µm). The HINC chamber reliability and uncertainty were calibrated by measuring the freezing of 200 nm ammonium nitrate particles at the same temperatures (*T*) as for soot particle IN experiments. To differentiate the phase of particles exiting HINC, we rely on comparing the *AF* curves of each soot sample in different OPC channels to those of 200 nm ammonium nitrate particles at the same *T*. Soluble ammonium nitrate particles only freeze when $T < HNT$ following the parameterization provided by Koop et al.[1] The *AF* curves of 200 nm ammonium nitrate aerosol particles in different OPC channels are presented in Fig. S1. The *AF* curves of 200 and 400 nm soot particles are shown in Figs. S2 to S13 and Figs. S14 to S25, respectively. At 243 K, the signal in OPC channels ≥ 3.0 µm is absent for all soot particles of 200 or 400 nm size, which is the same as for 200 nm ammonium nitrate particles confirming only forming water droplets of sizes smaller than 3.0 µm at the same conditions. As such we can be confident that no IN is detected for our soot particles at $T = 243$ K since no signal appears in the channels ≥ 3.0 µm as ice crystals would grow to larger sizes in the given residence time. Similarly, fresh and denuded mCASTblack, mCASTblack and PR90, as well as fresh FW200 soot particles cannot form ice crystals at 238 K. By the same reasoning, we judge that denuded 200 nm FW200 soot particles may not nucleate ice at 238 K (see Figs. S21 and S22). However, when $RH_w > 105\%$ at 238 K, the *AF* curves of denuded 400 nm FW200-N_2 and FW200-air soot particles in OPC channels ≥ 4.0 µm can reach an *AF* value higher than 10^{-3} which ammonium nitrate particles cannot (see Figs. S9 and S10). Because ice crystals grow more efficiently than water droplets at the same condition,[2,3] we believe that some ice crystals are in present for the cases of 400 nm FW200-N_2 and FW200-air soot particles at 238 K. When $T < 238$ K, it cannot be excluded that particles exiting HINC in OPC channels ≥ 1.0 µm are in ice phase.

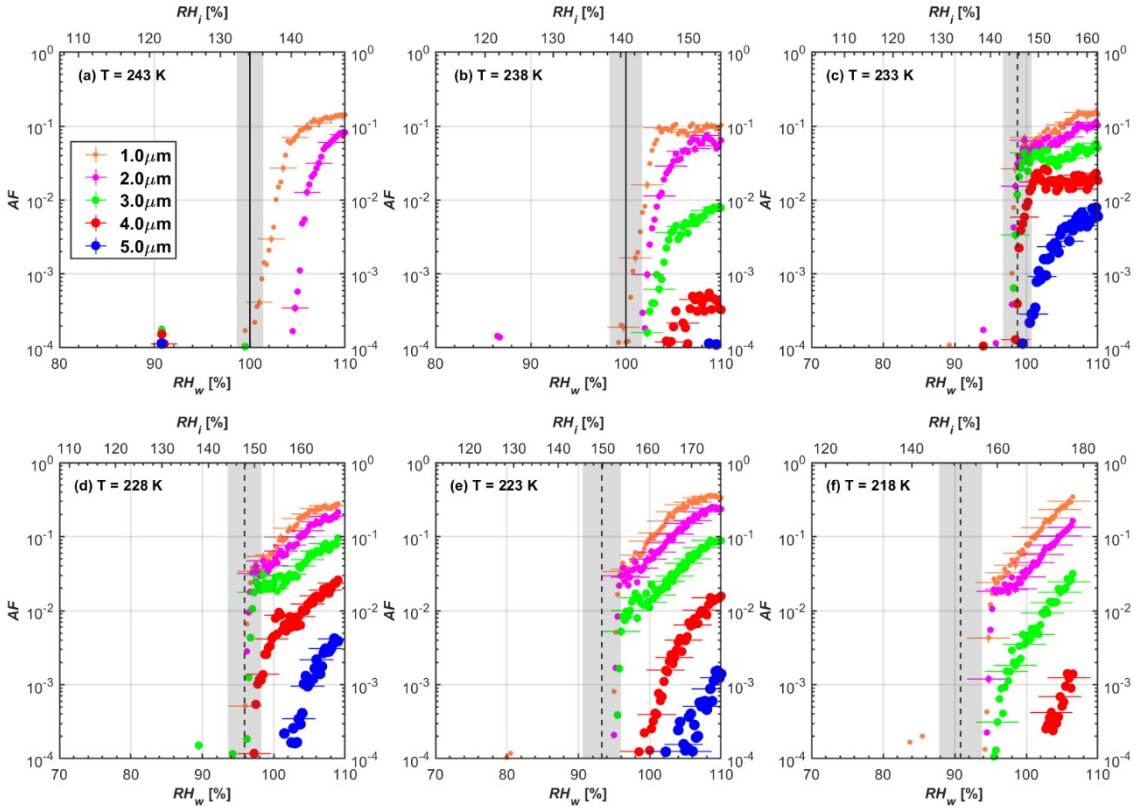

Figure S1. AF as a function of RH for 200 nm ammonium nitrate corresponding to 1.0, 2.0, 3.0, 4.0 and 5.0 µm OPC channels. Black solid lines represent water saturation conditions according to Murphy and Koop. [4] Black dashed lines denote the expected RH values for homogeneous freezing at T < HNT.[1] The grey shading shows the possible RH uncertainty calculated for water saturation and homogeneous freezing conditions.

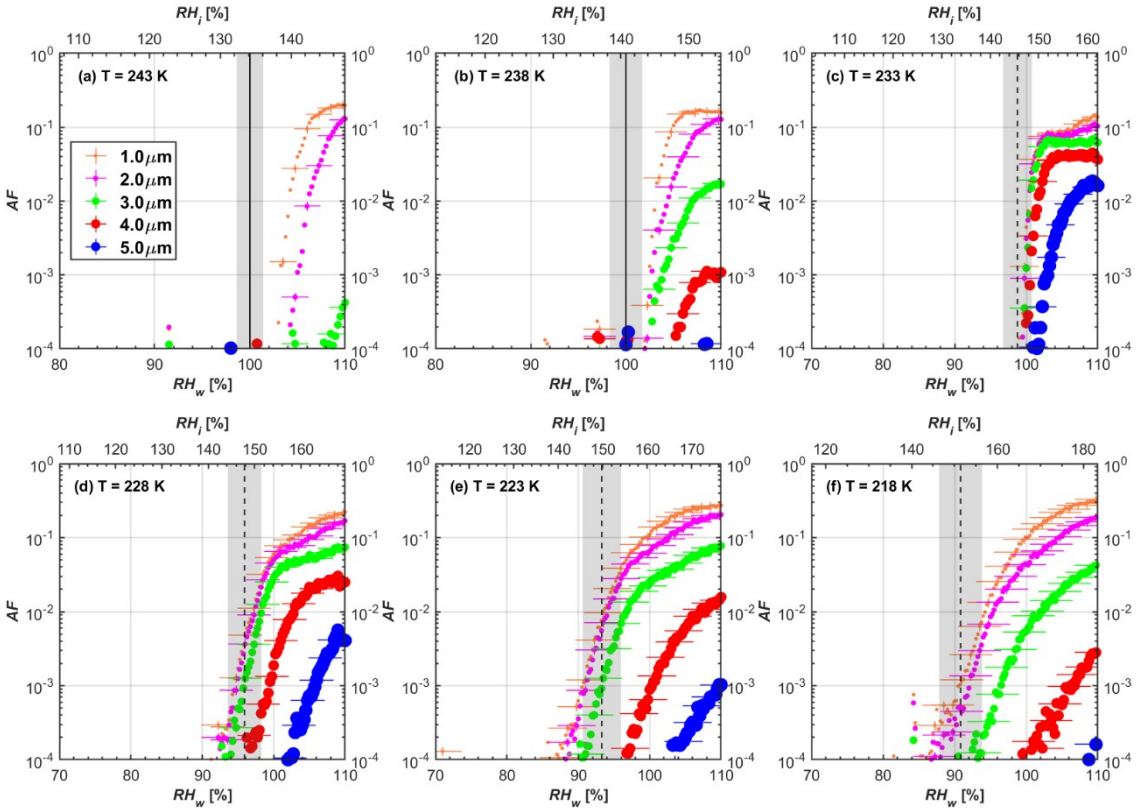

Figure S2. Same as Fig. S1 but for 400 nm mCASTblack soot particles.

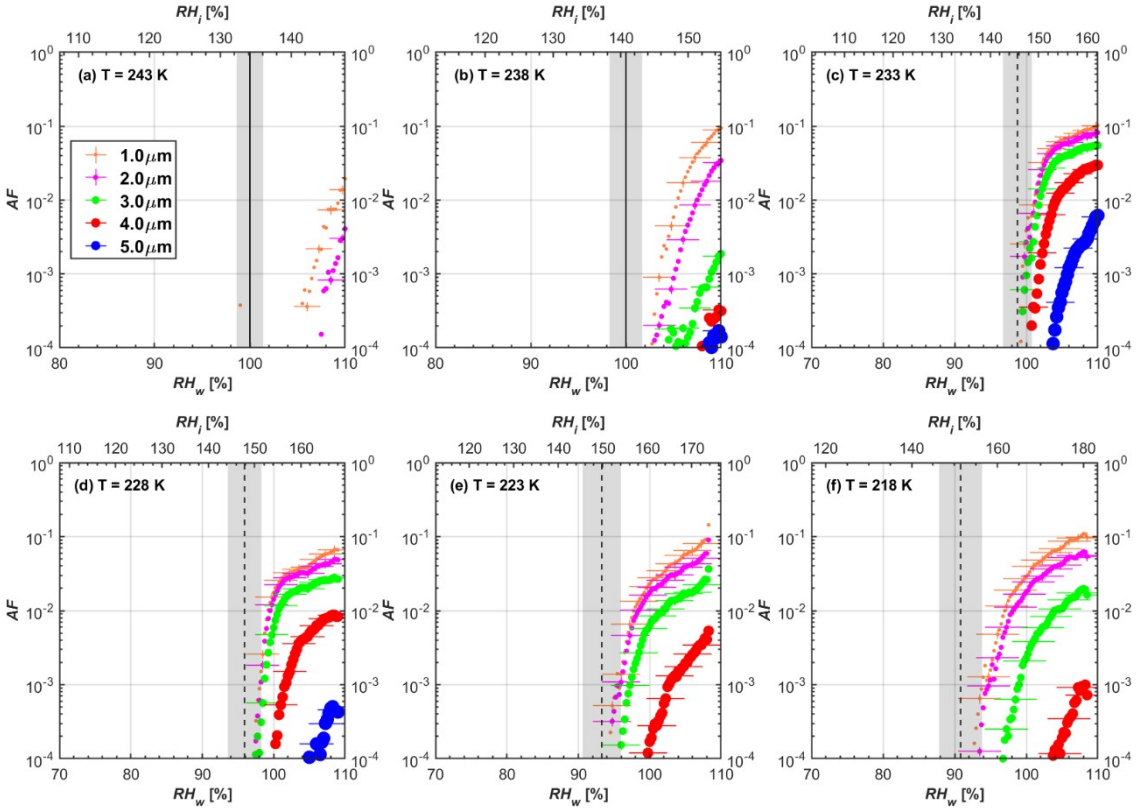

Figure S3. Same as Fig. S1 but for 400 nm mCASTblack-N_2 soot particles.

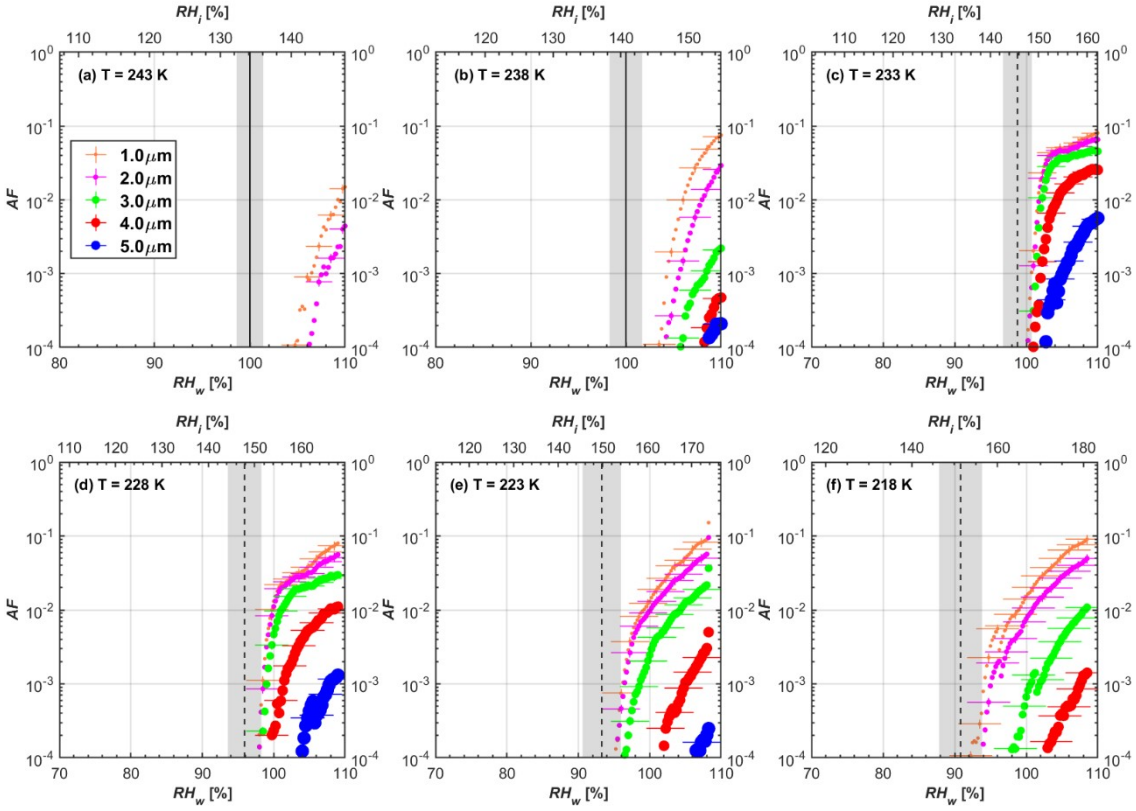

Figure S4. Same as Fig. S1 but for 400 nm mCASTblack-air soot particles.

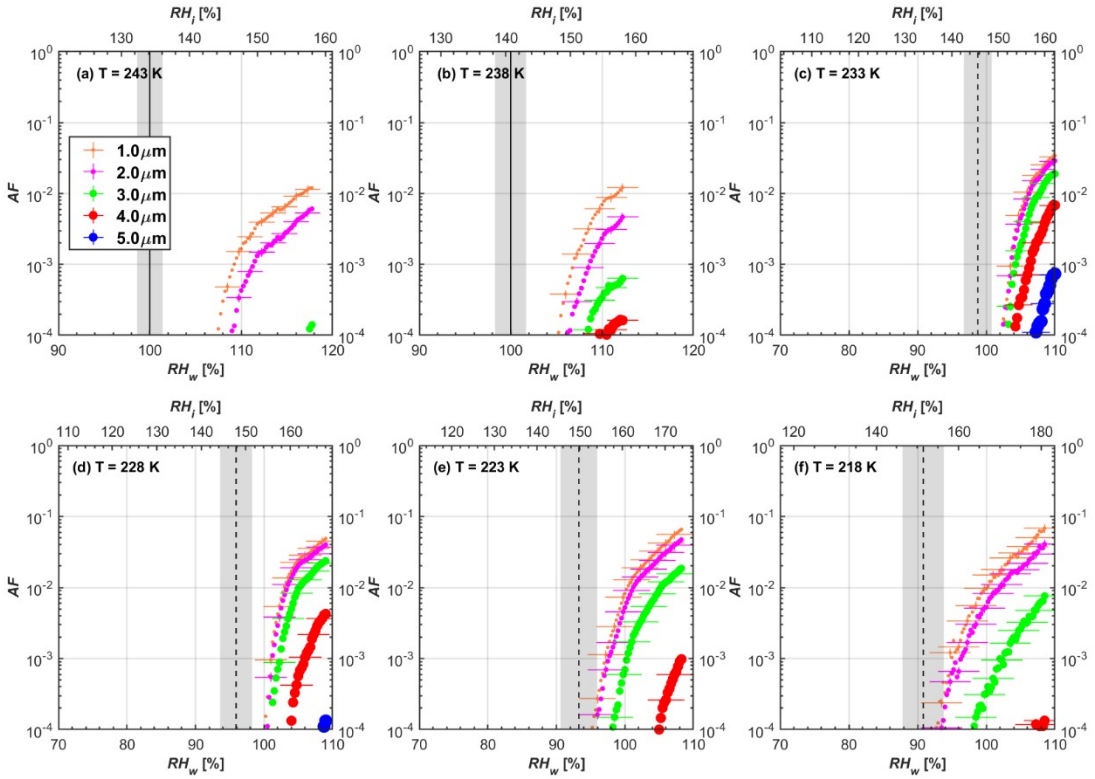

Figure S5. Same as Fig. S1 but for 400 nm mCASTbrown soot particles.

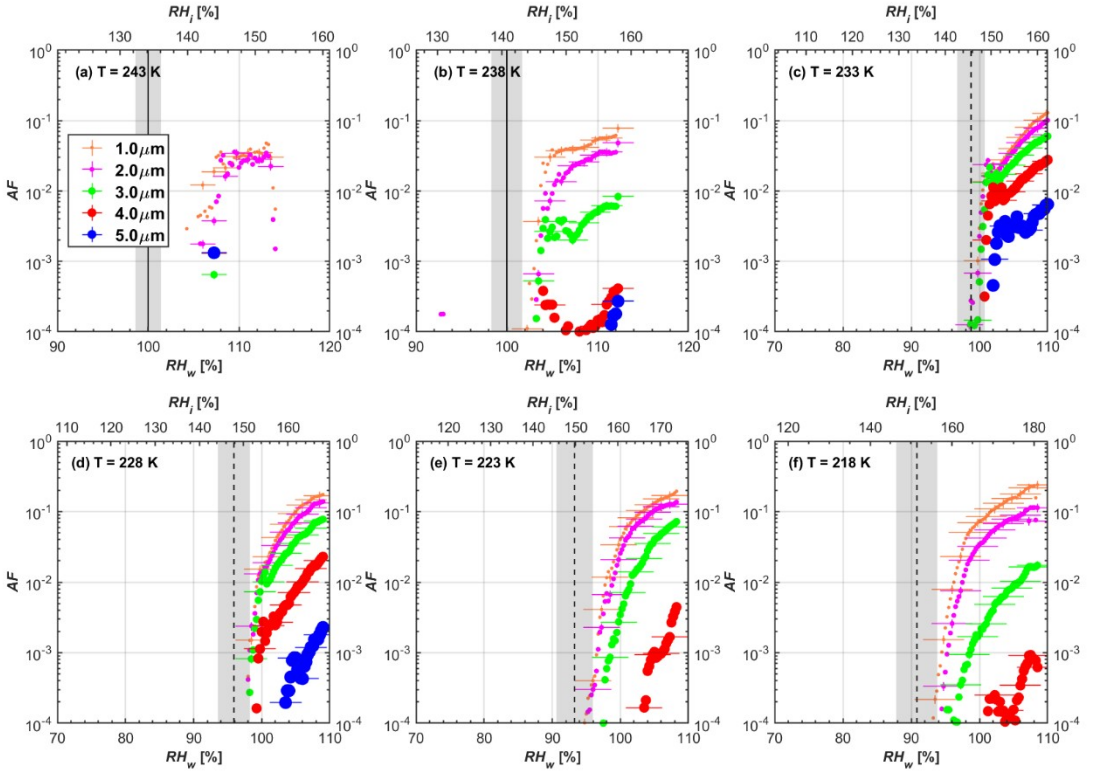

Figure S6. Same as Fig. S1 but for 400 nm mCASTbrown-N_2 soot particles.

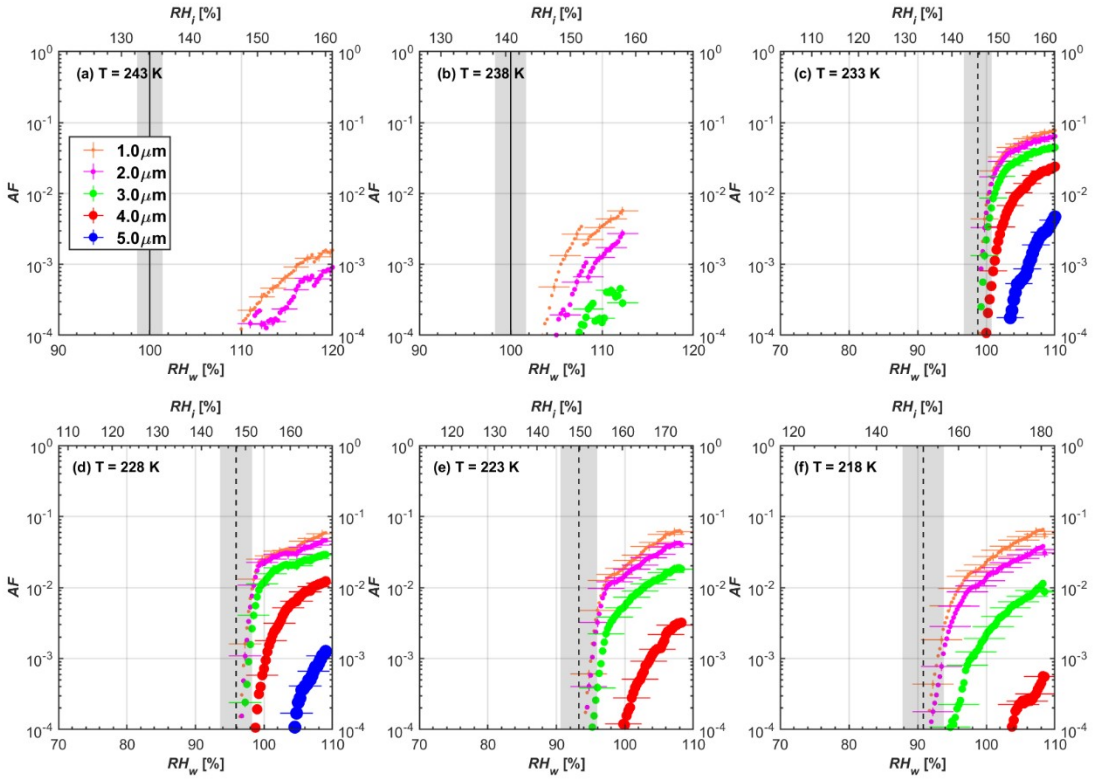

Figure S7. Same as Fig. S1 but for 400 nm mCASTbrown-air soot particles.

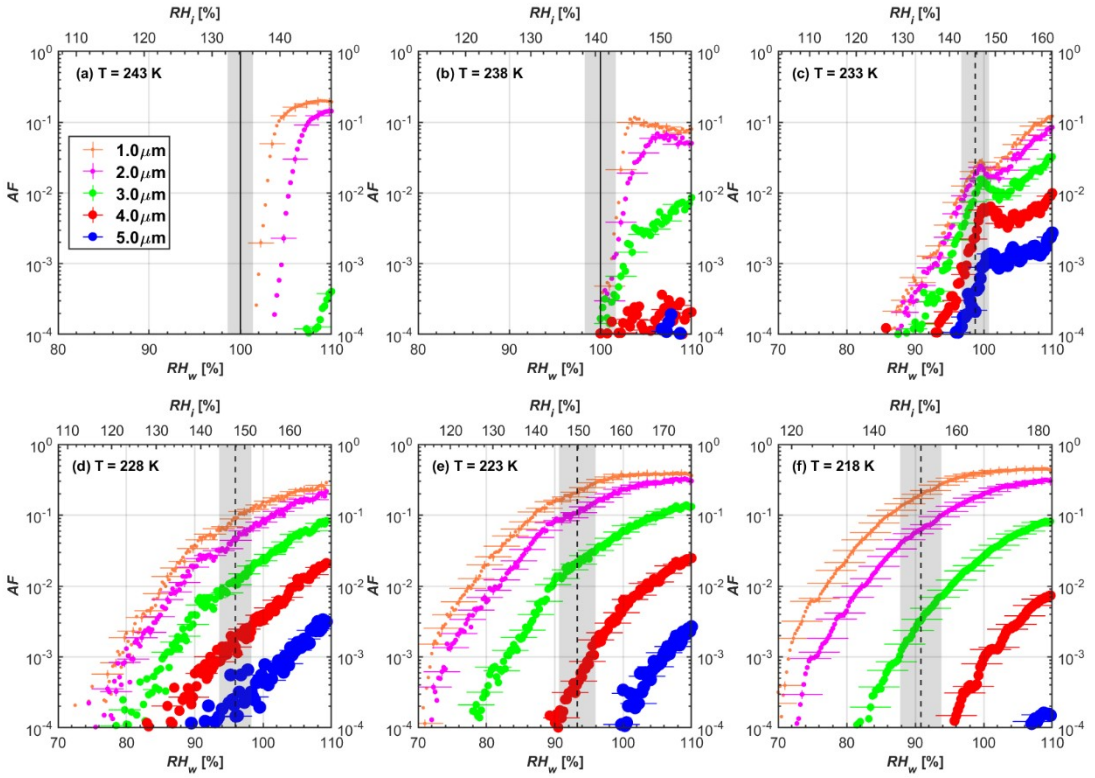

Figure S8. Same as Fig. S1 but for 400 nm FW200 soot particles.

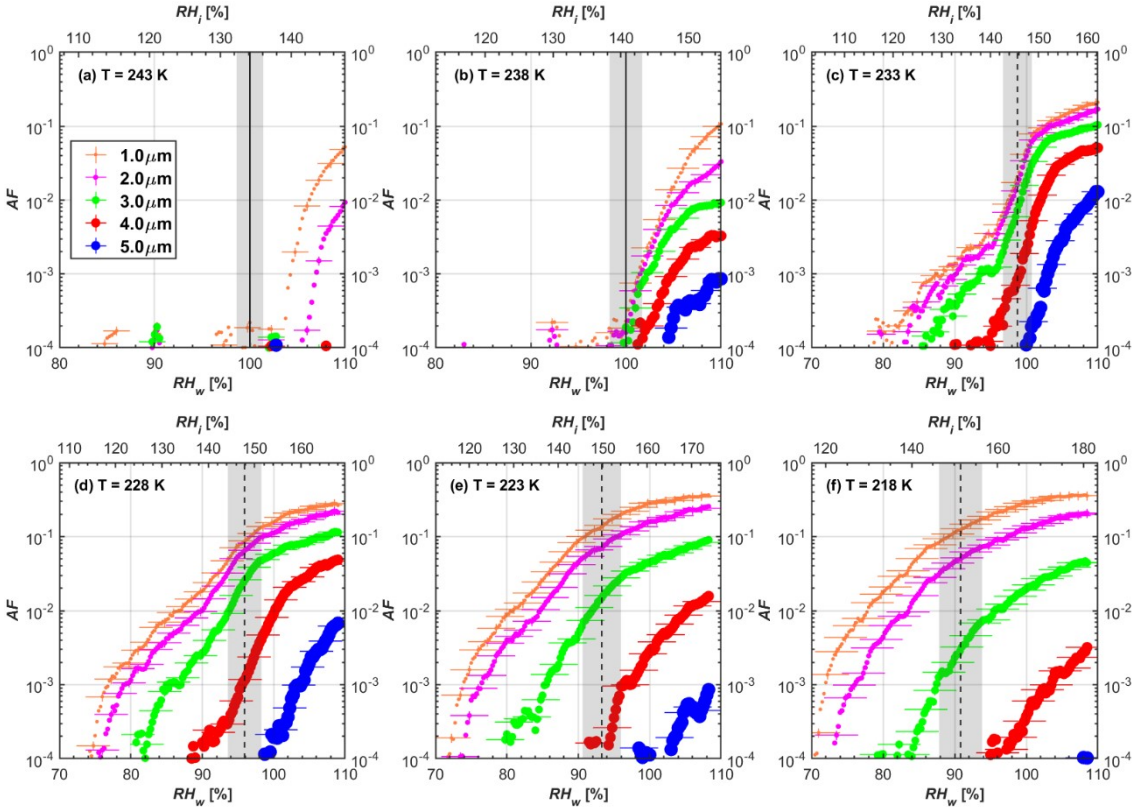

Figure S9. Same as Fig. S1 but for 400 nm FW200-N_2 soot particles.

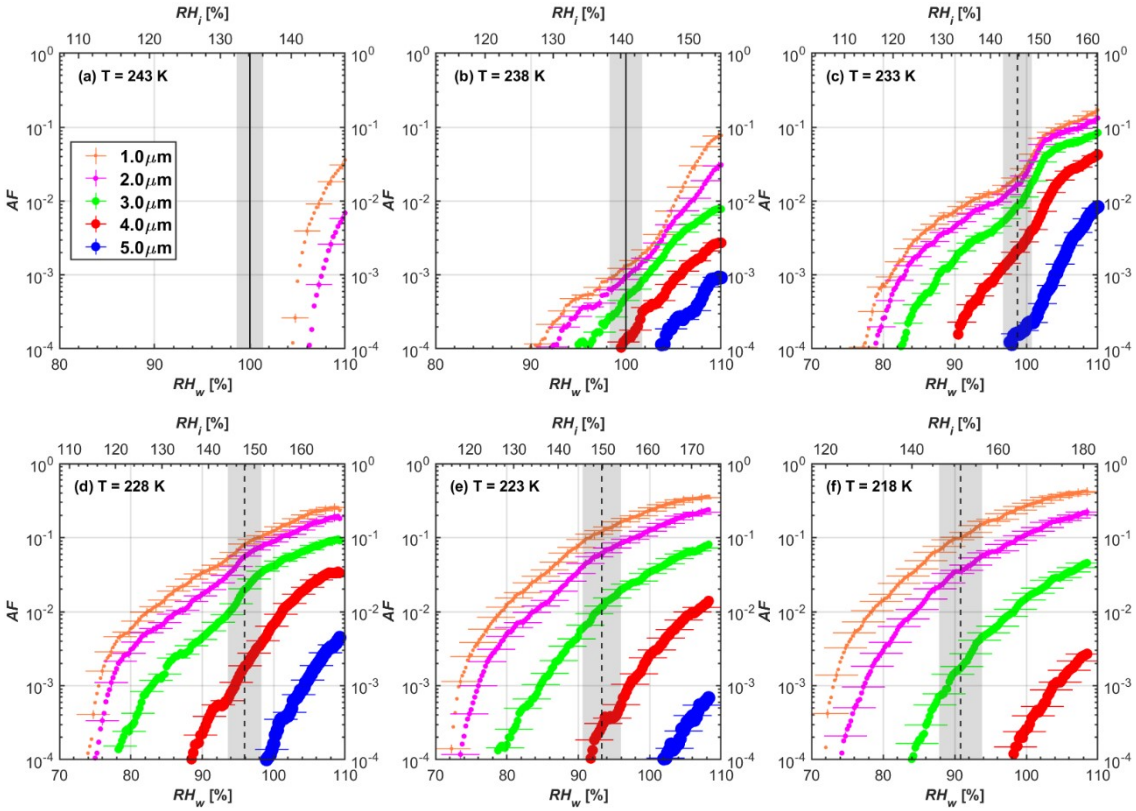

Figure S10. Same as Fig. S1 but for 400 nm FW200-air soot particles.

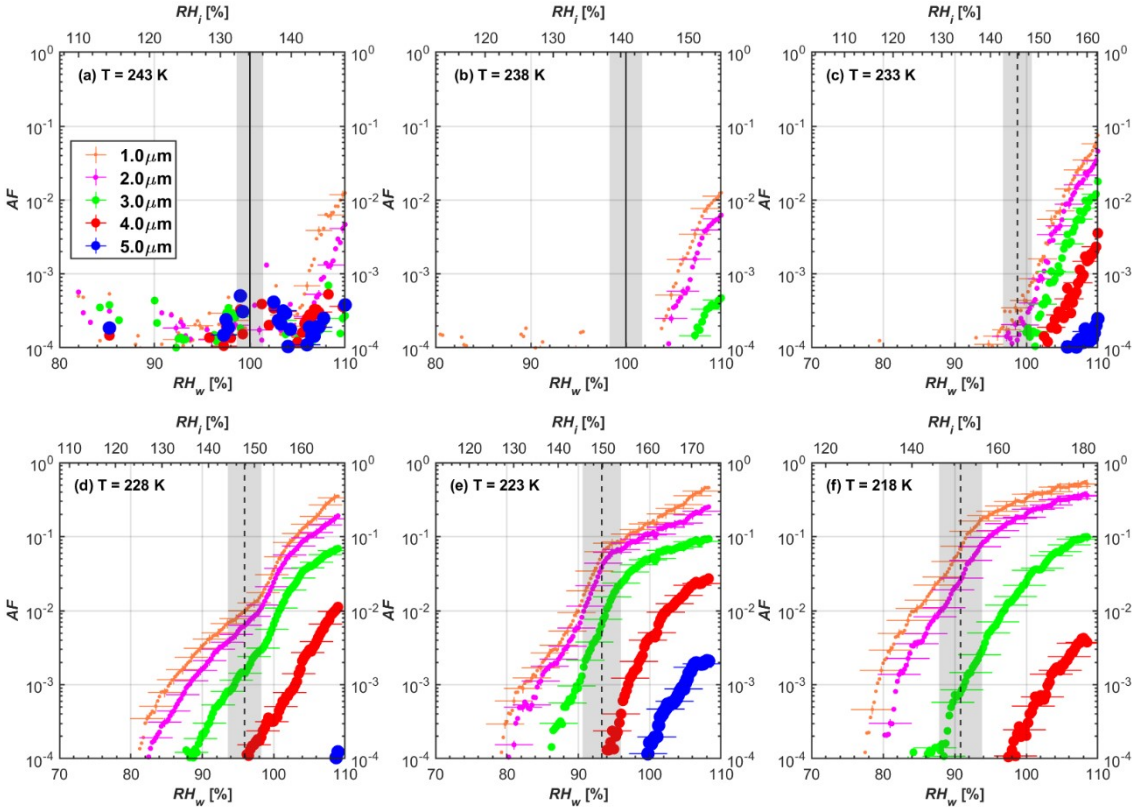

Figure S11. Same as Fig. S1 but for 400 nm PR90 soot particles.

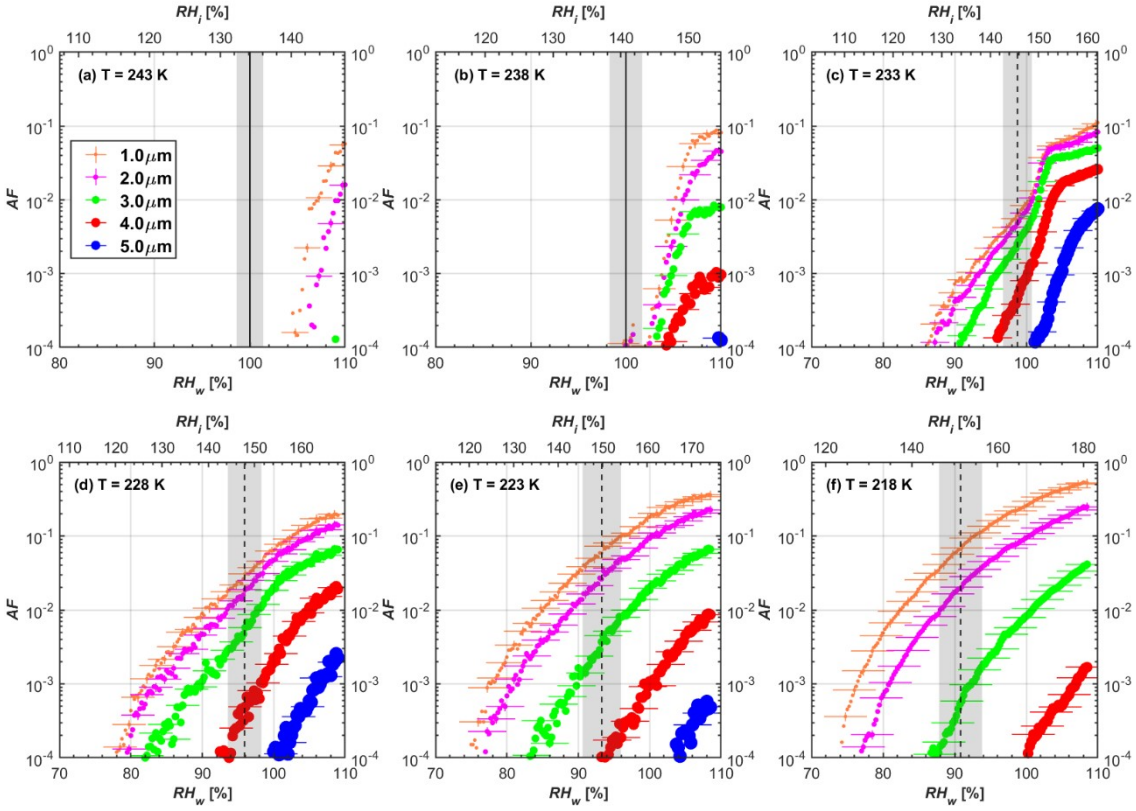

Figure S12. Same as Fig. S1 but for 400 nm PR90-N_2 soot particles.

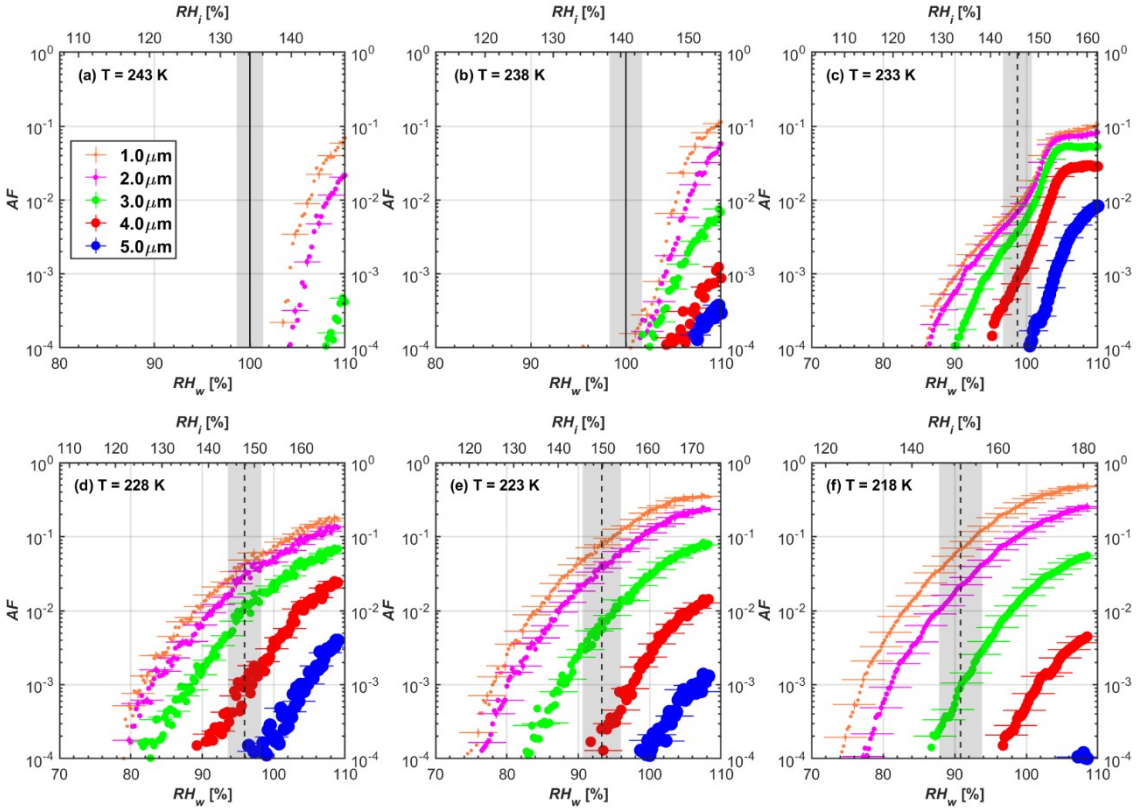

Figure S13. Same as Fig. S1 but for 400 nm PR90-air soot particles.

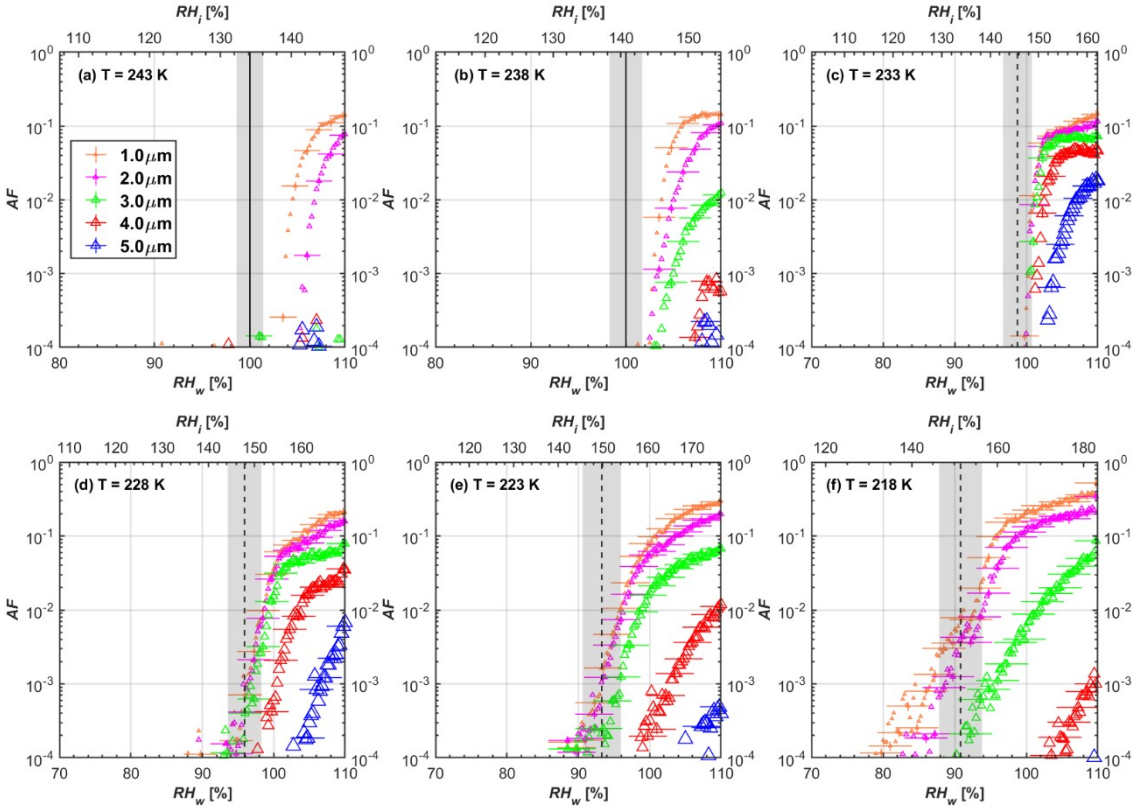

Figure S14. Same as Fig. S1 but for 200 nm mCASTblack soot particles.

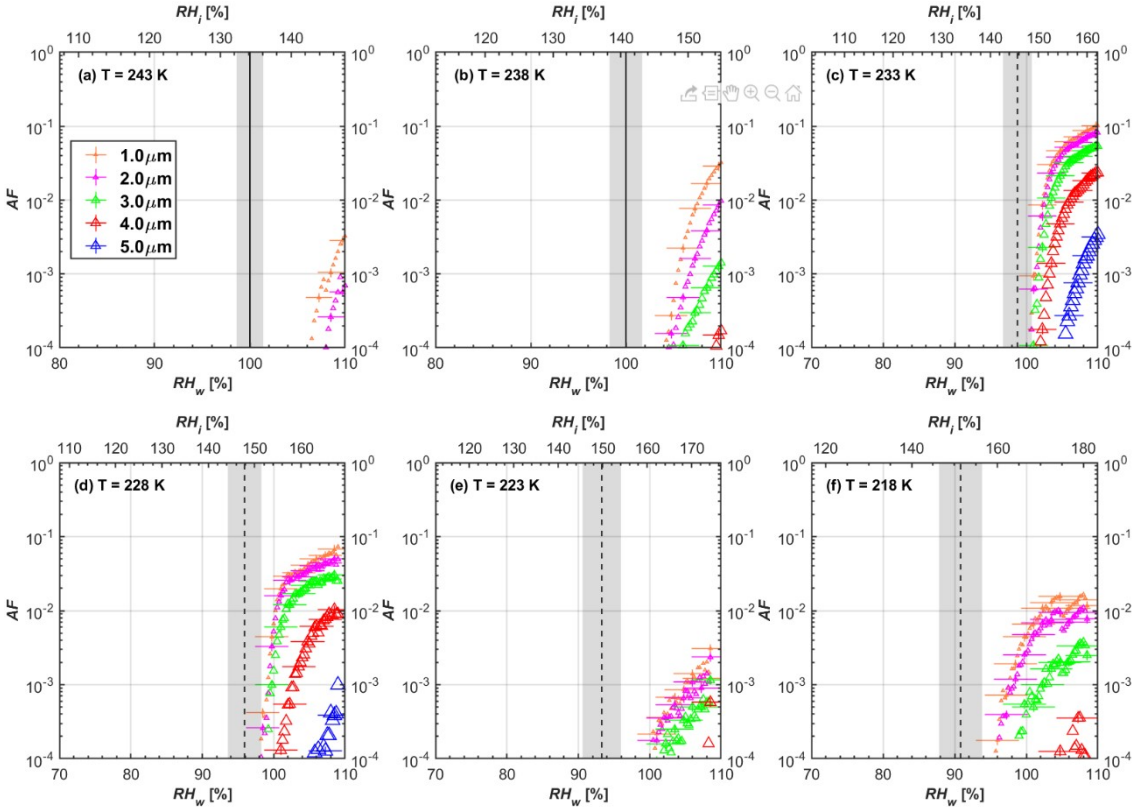

Figure S15. Same as Fig. S1 but for 200 nm mCASTblack-N_2 soot particles.

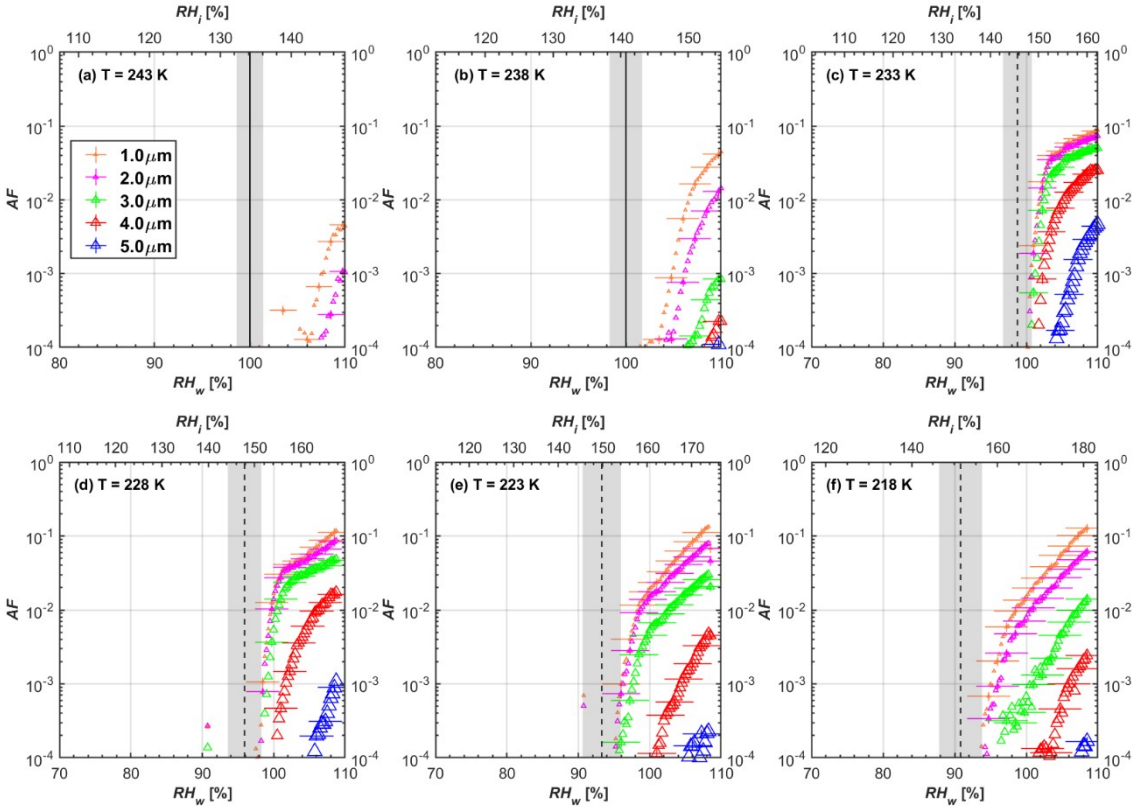

Figure S16. Same as Fig. S1 but for 200 nm mCASTblack-air soot particles.

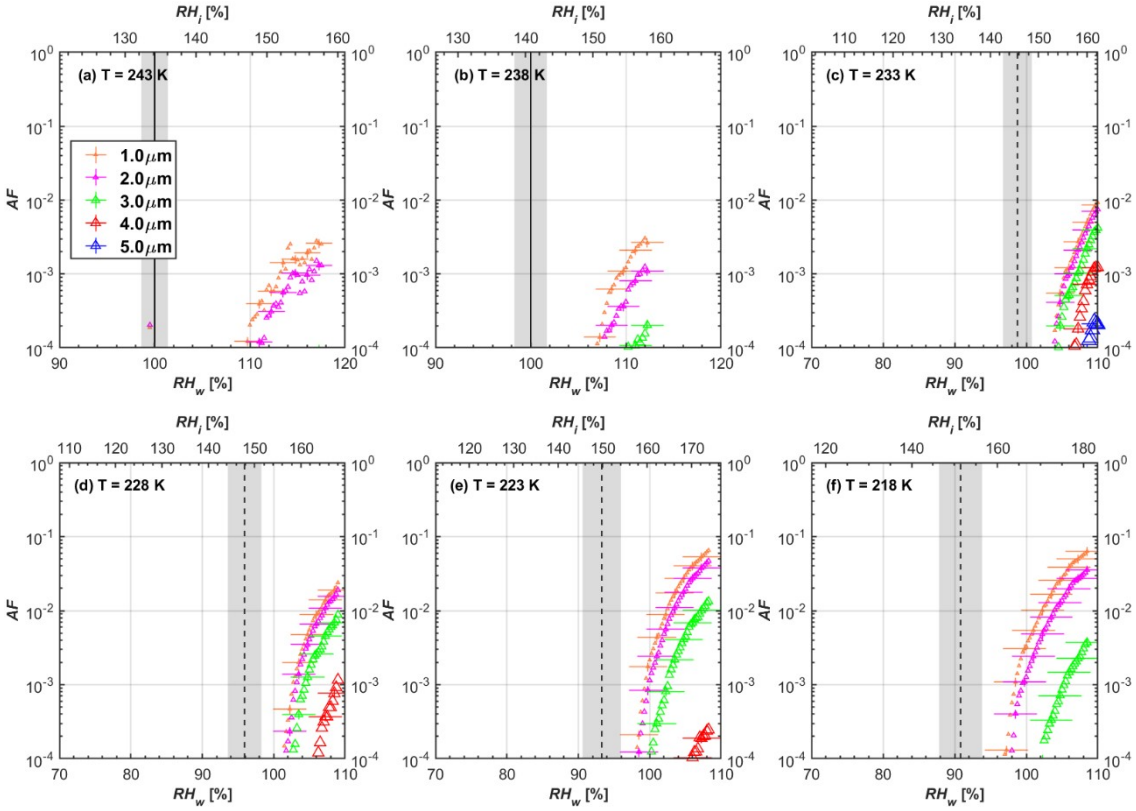

Figure S17. Same as Fig. S1 but for 200 nm mCASTbrown soot particles.

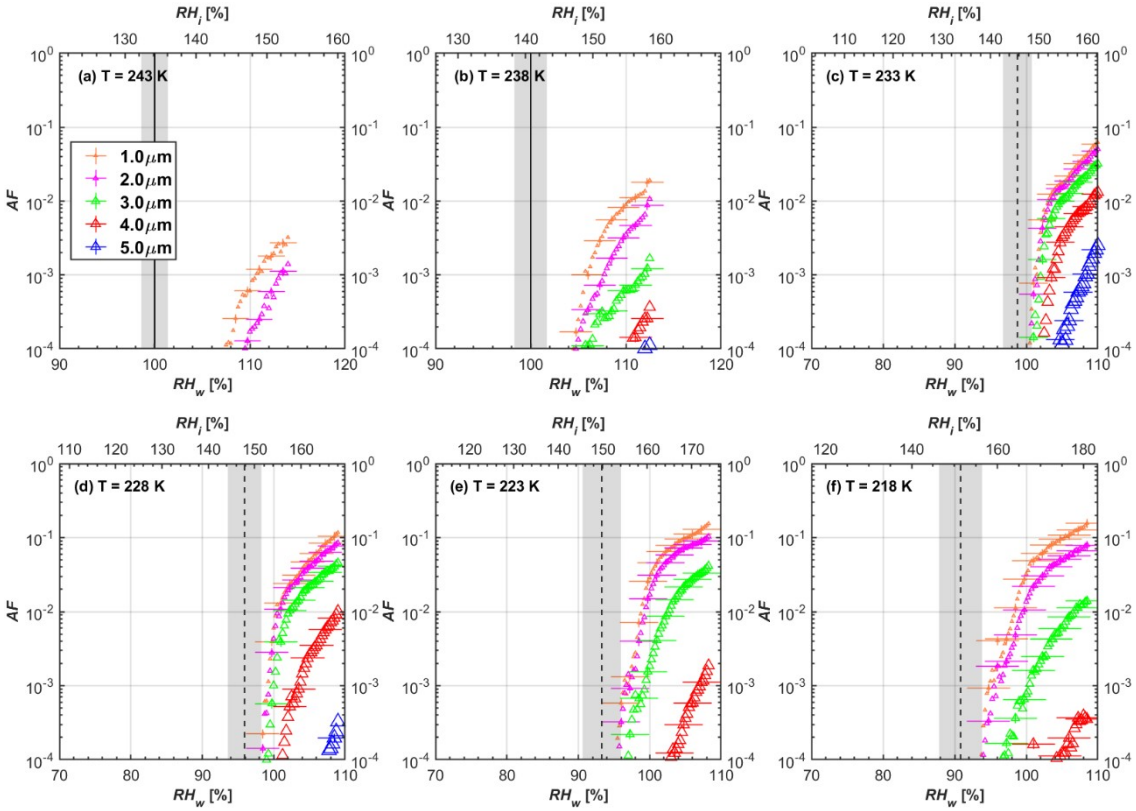

Figure S18. Same as Fig. S1 but for 200 nm mCASTbrown-N_2 soot particles.

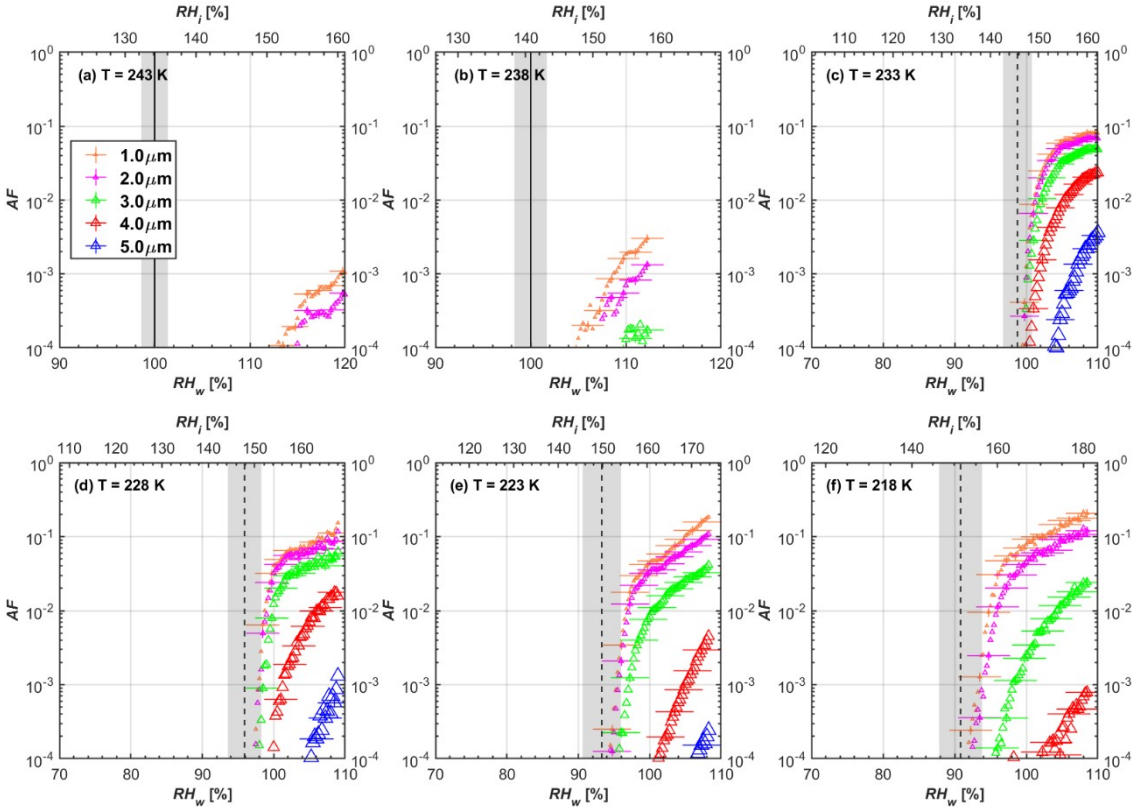

Figure S19. Same as Fig. S1 but for 200 nm mCASTbrown-air soot particles.

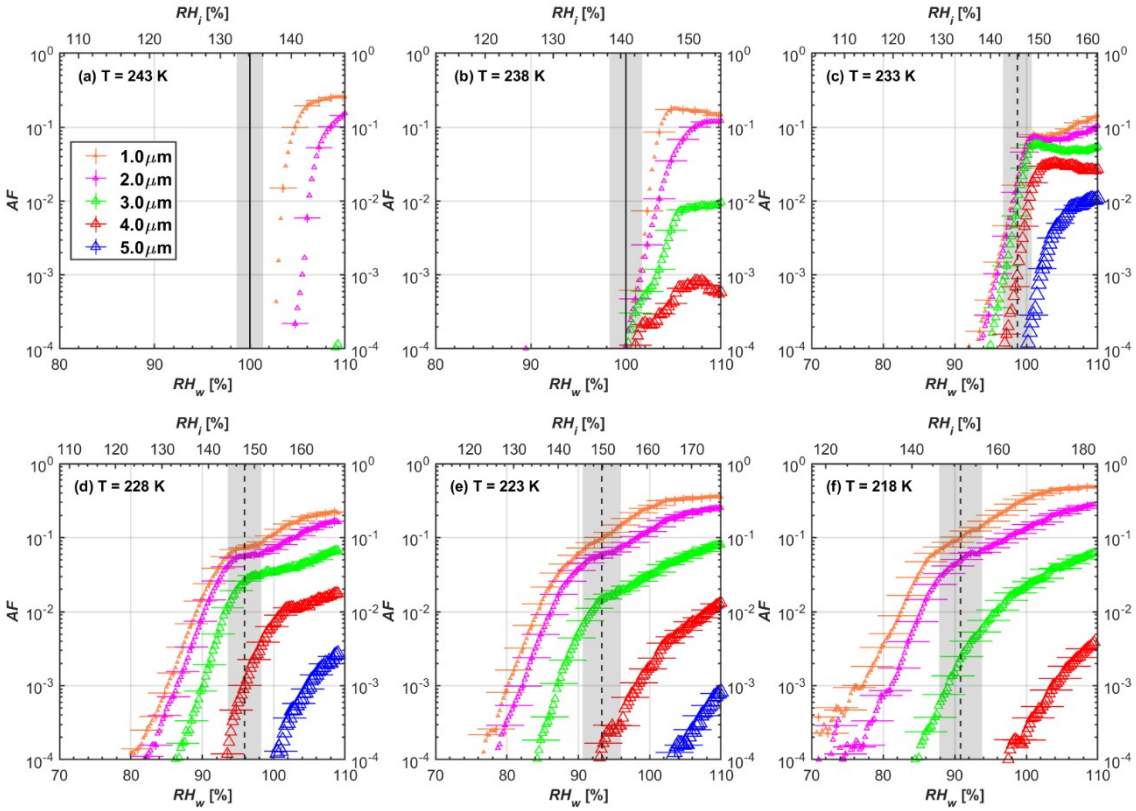

Figure S20. Same as Fig. S1 but for 200 nm FW200 soot particles.

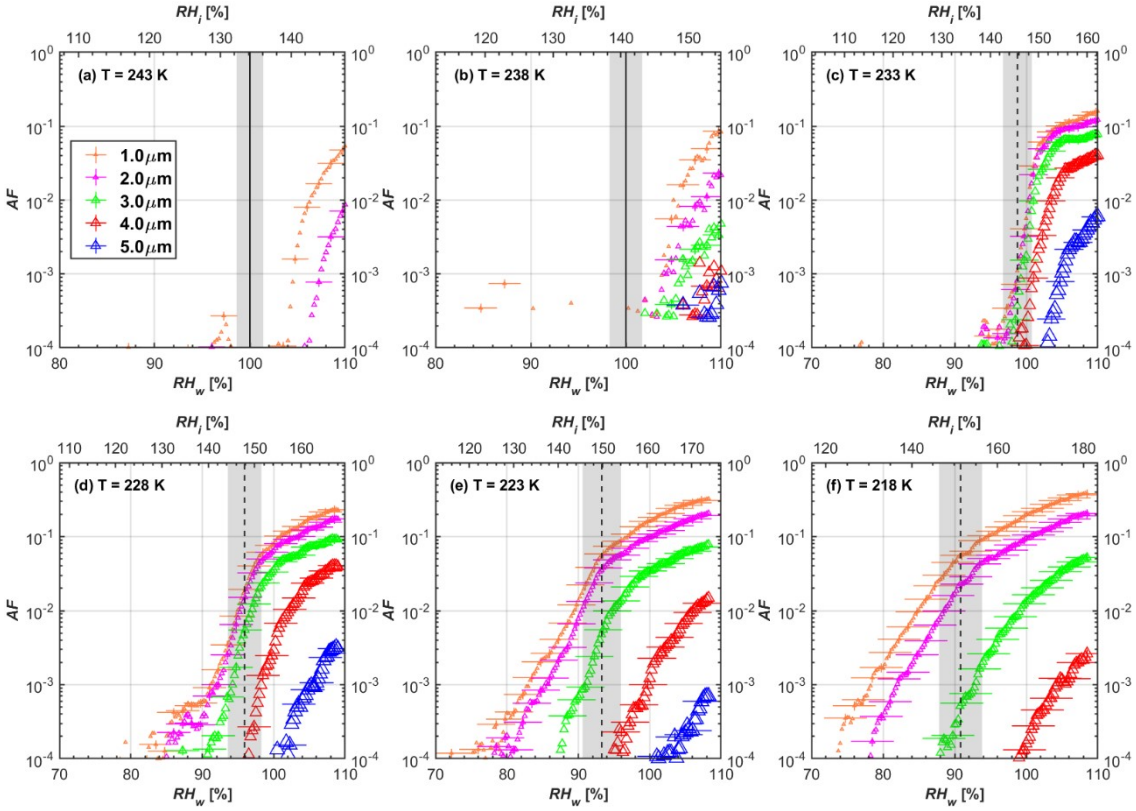

Figure S21. Same as Fig. S1 but for 200 nm FW200-N_2 soot particles.

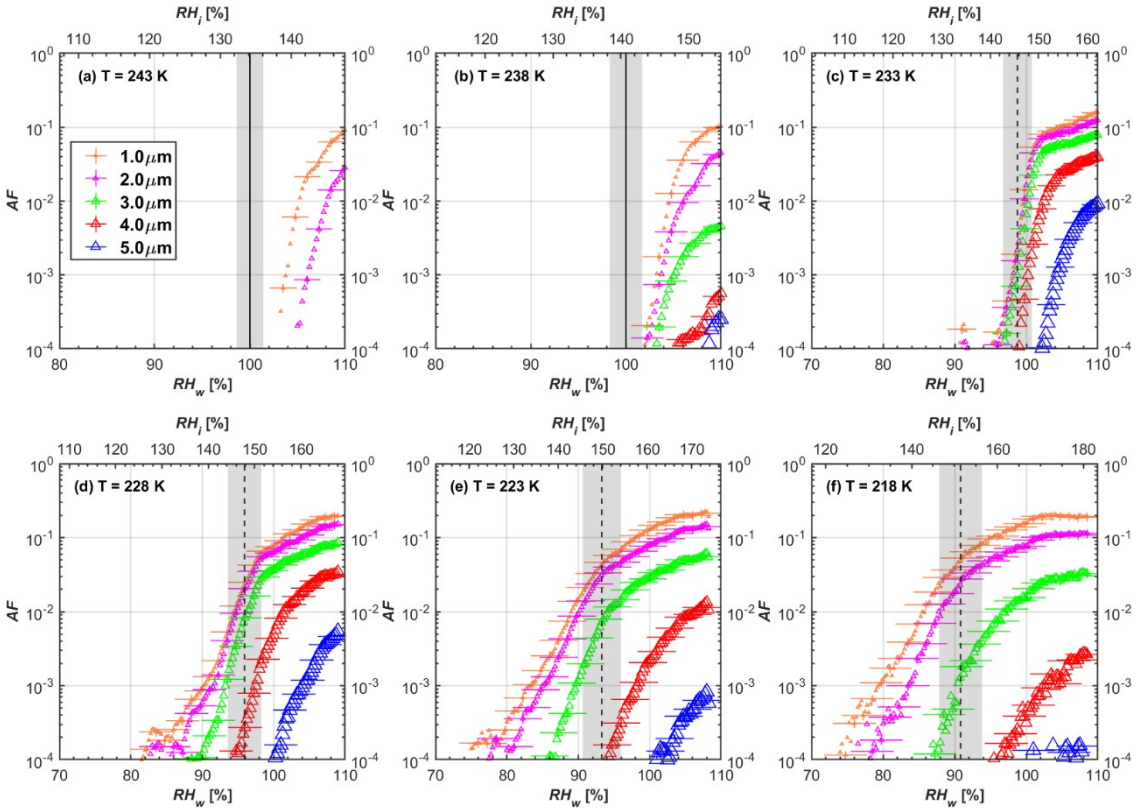

Figure S22. Same as Fig. S1 but for 200 nm FW200-air soot particles.

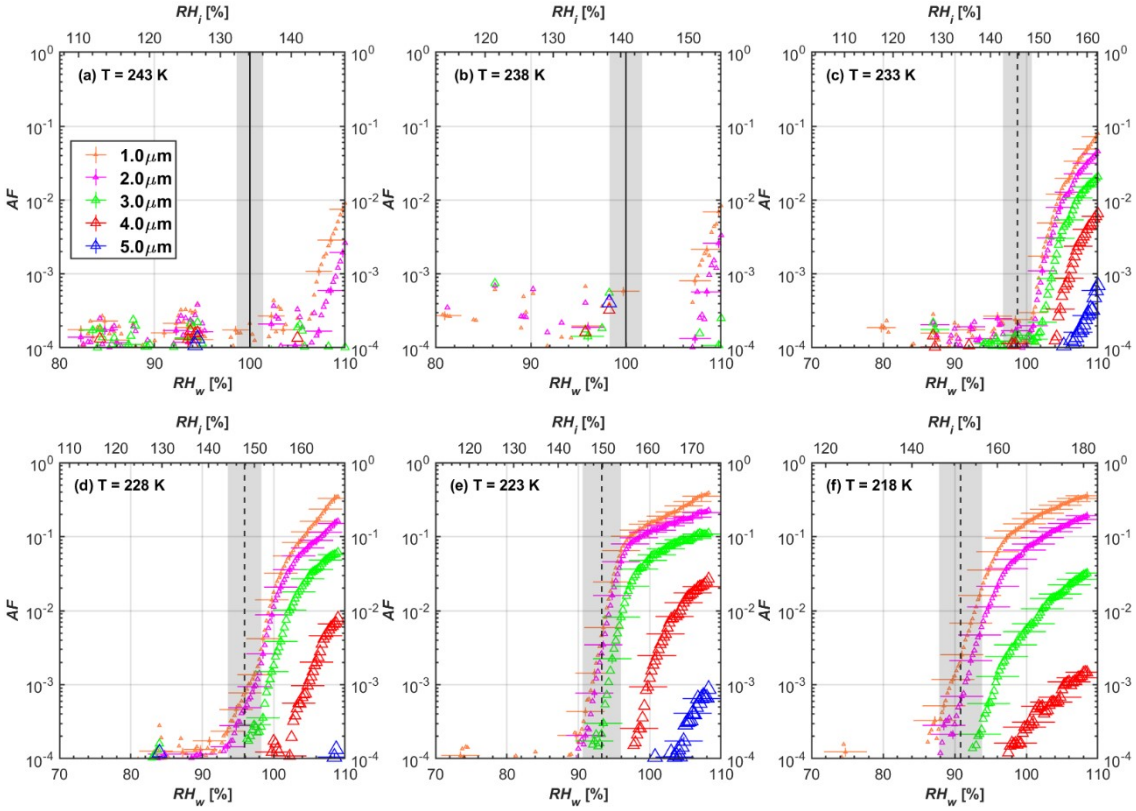

Figure S23. Same as Fig. S1 but for 200 nm PR90 soot particles.

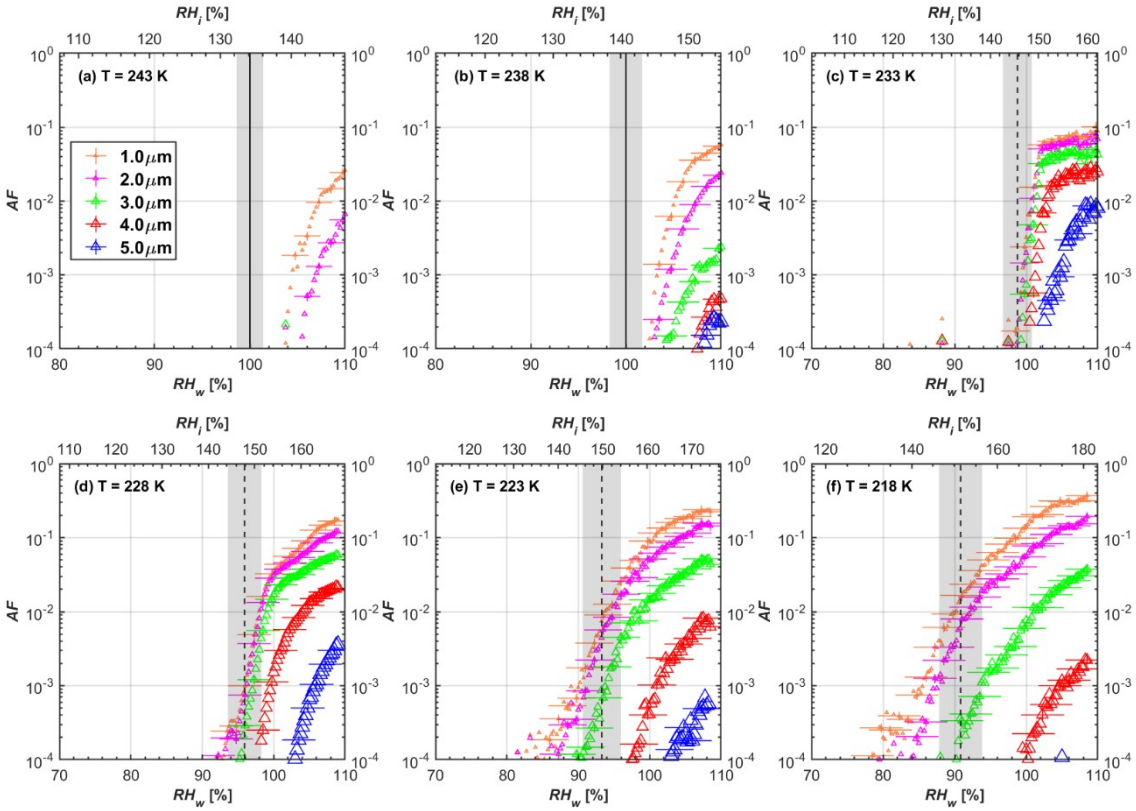

Figure S24. Same as Fig. S1 but for 200 nm PR90-N_2 soot particles.

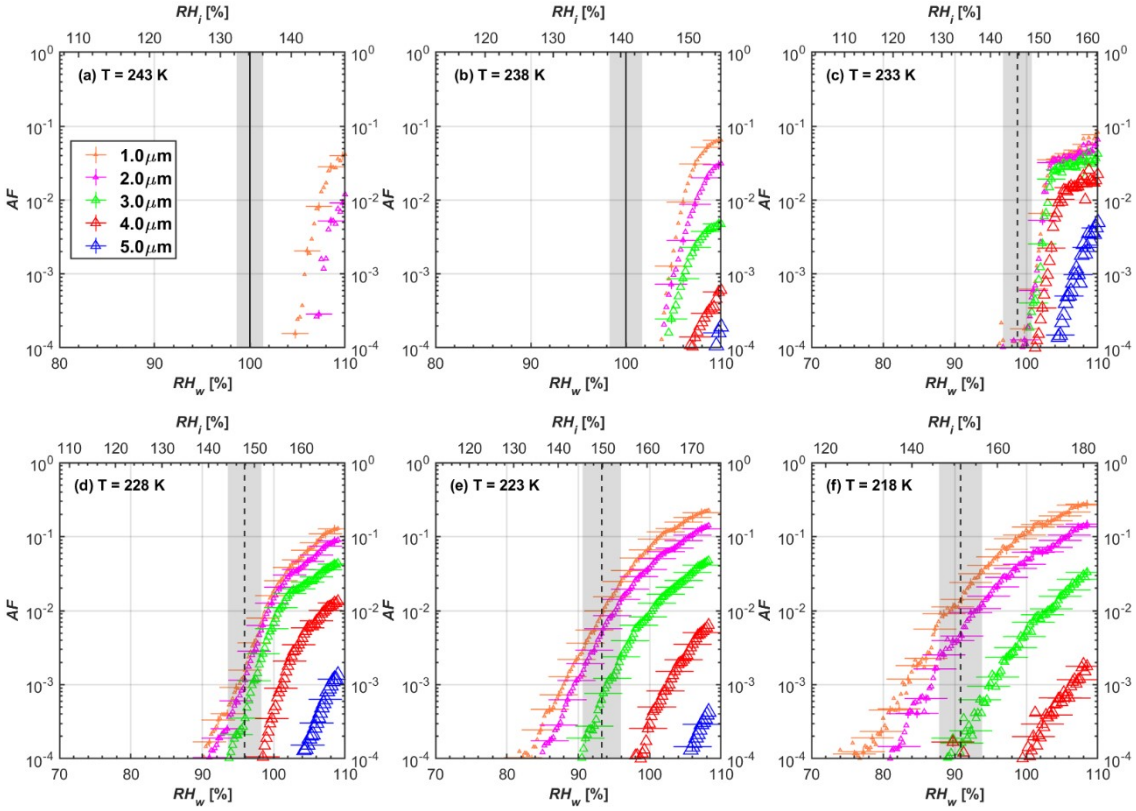

Figure S25. Same as Fig. S1 but for 200 nm PR90-air soot particles.

S2 Particle size and mass distribution for size selected soot aerosols

The particle size and mass distribution for the soot samples are shown in Figs. S26 to S33 with their corresponding log-normal fit curves. To verify the size selection quality of the DMA (Differential Mobility Analyser), the multiple charged particle percentage of the size-selected soot aerosols is derived from the SMPS (Scanning Mobility Particle Sizer) measurement with turning on multiple charge correction for data processing. The DMA was running with a sheath to aerosol flow ratio of 13 : 1 and 7.3 : 1 for 200 and 400 nm soot particle size selection, respectively. The CPC (Condensation Particle Counter) 3776 pulled downstream of the SMPS running in low flow mode with a flow rate of 0.3 L min^{-1}. The sheath to aerosol flow ratios through the SMPS used to confirm the size selection quality for 200 and 400 nm size-selected soot particles were set to 3.0 : 0.3 and 1.8 : 0.3, respectively. As indicated in Figs. S26, S28, S30 and S32, the multiple charged particles exhibit approximately 10-20% of the soot sample particle population, showing larger sizes than the size selection value (see figure legend for detailed values). Additionally, thermal denuding does not affect the soot aerosol sample size selection quality, as shown that the percentage of double-charged soot particles does not change significantly for the same soot sample group.

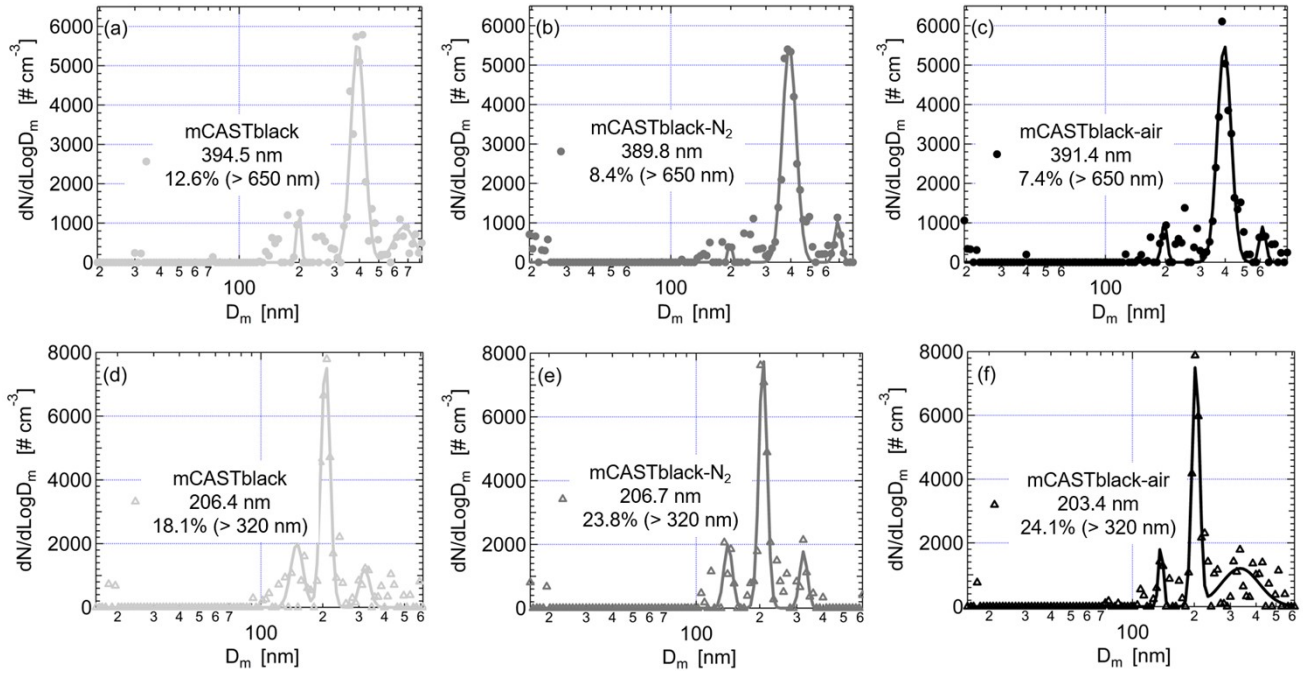

Figure S26. The size distribution of fresh and denuded 400 (a, b, c) and 200 nm (d, e, f) size-selected mCASTblack soot particles. The lognormal fitting derived size mode values are shown in brackets for each soot sample. Raw data points are indicated by round (400 nm) or triangle (200 nm) symbols. Solid lines are lognormal fit curves. The size distribution mode value, the multiple charged particle percentage are indicated in the legend, respectively.

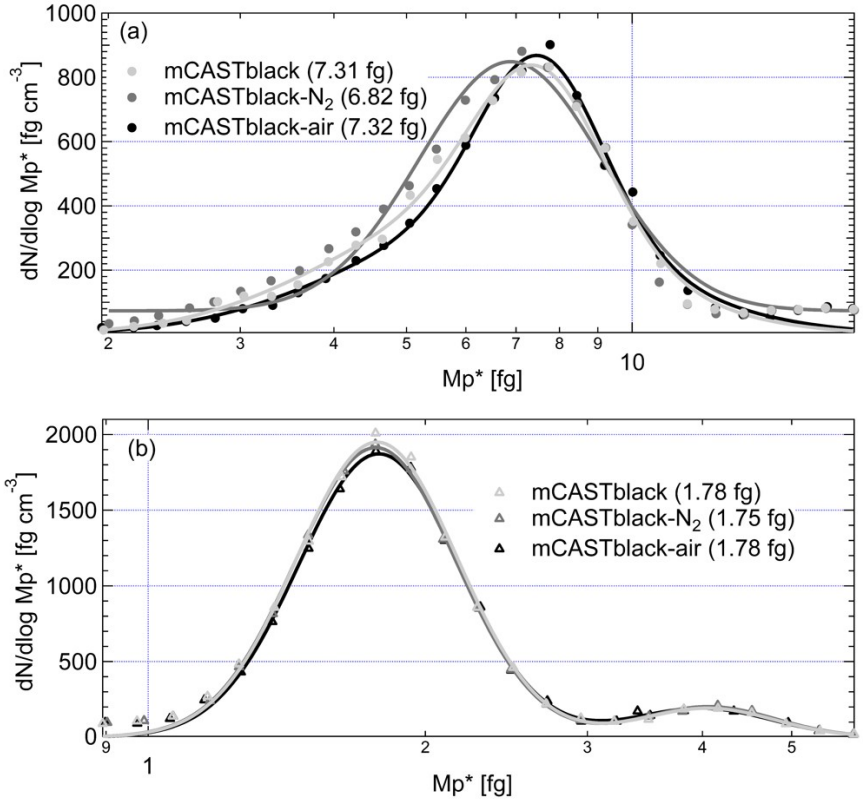

Figure S27. The mass distribution of fresh and denuded 400 (a) and 200 nm (b) size-selected mCASTblack soot particles. Symbols and lines as in Fig. S26.

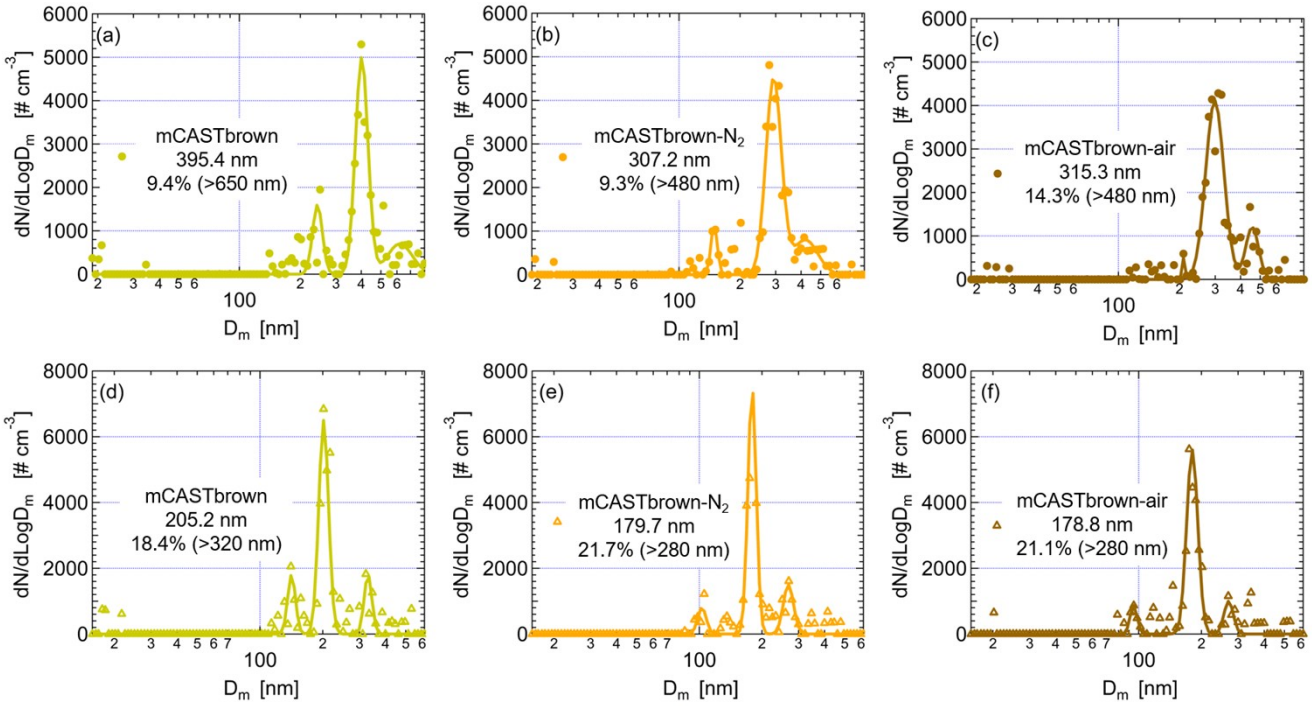

Figure S28. The size distribution of fresh and denuded 400 (a, b, c) and 200 nm (d, e, f) size-selected mCASTbrown soot particles. Symbols and lines as in Fig. S26.

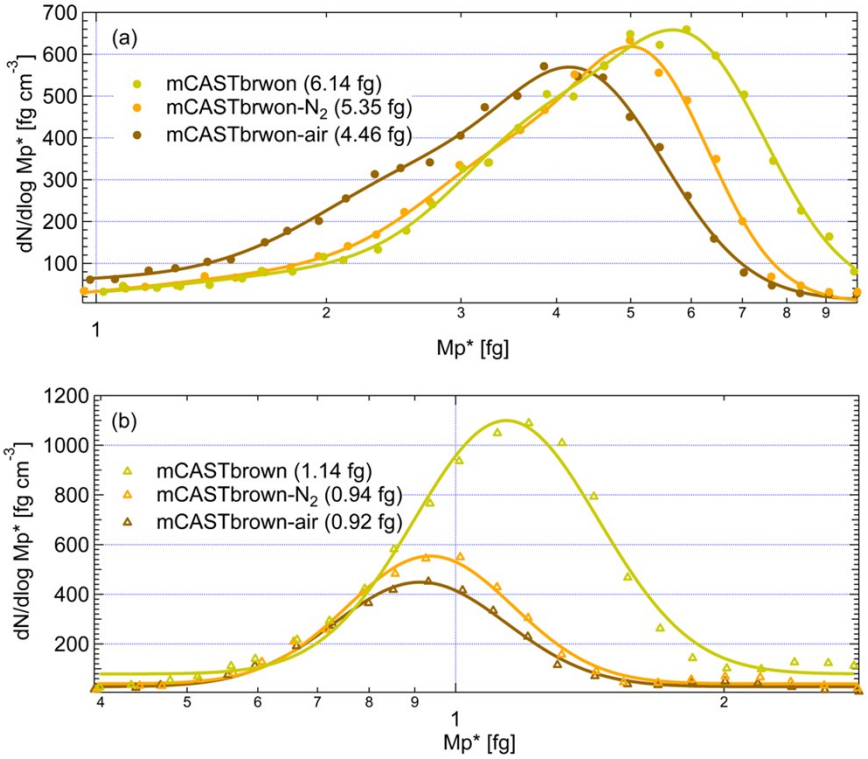

Figure S29. The mass distribution of fresh and denuded 400 (a) and 200 nm (b) size-selected mCASTbrown soot particles. Symbols and lines as in Fig. S26.

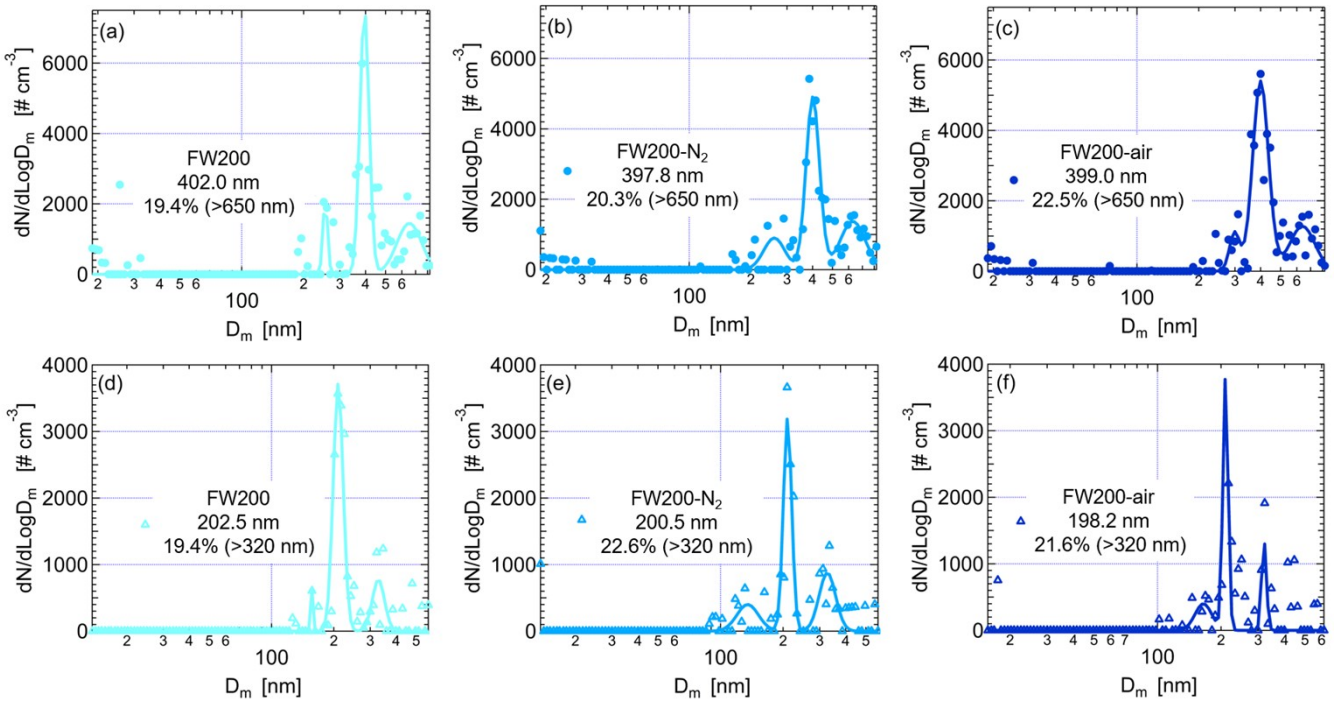

Figure S30. The size distribution of fresh and denuded 400 (a, b, c) and 200 nm (d, e, f) size-selected FW200 soot particles. Symbols and lines as in Fig. S26.

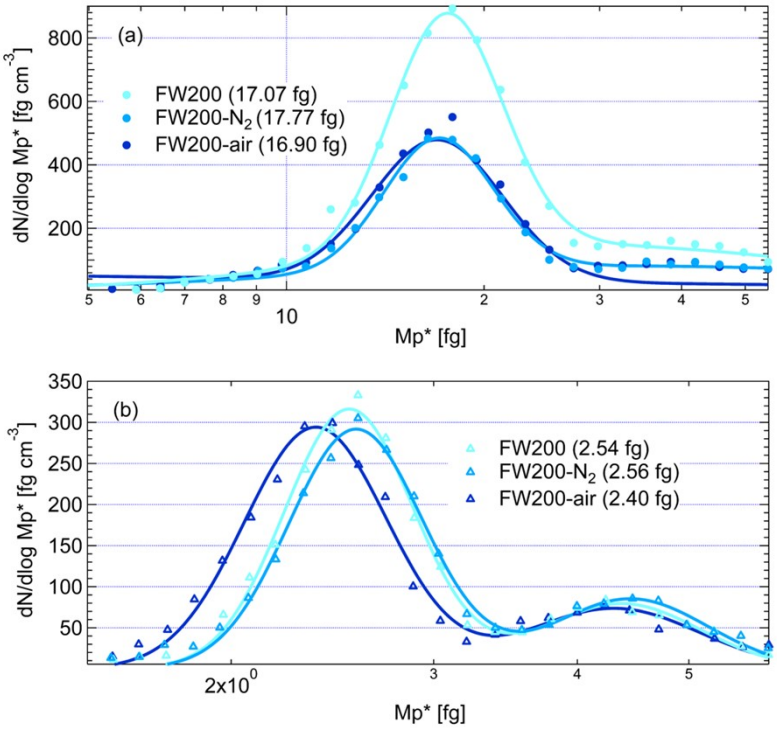

Figure S31. The mass distribution of fresh and denuded 400 (a) and 200 nm (b) size-selected FW200 soot particles. Symbols and lines as in Fig. S26.

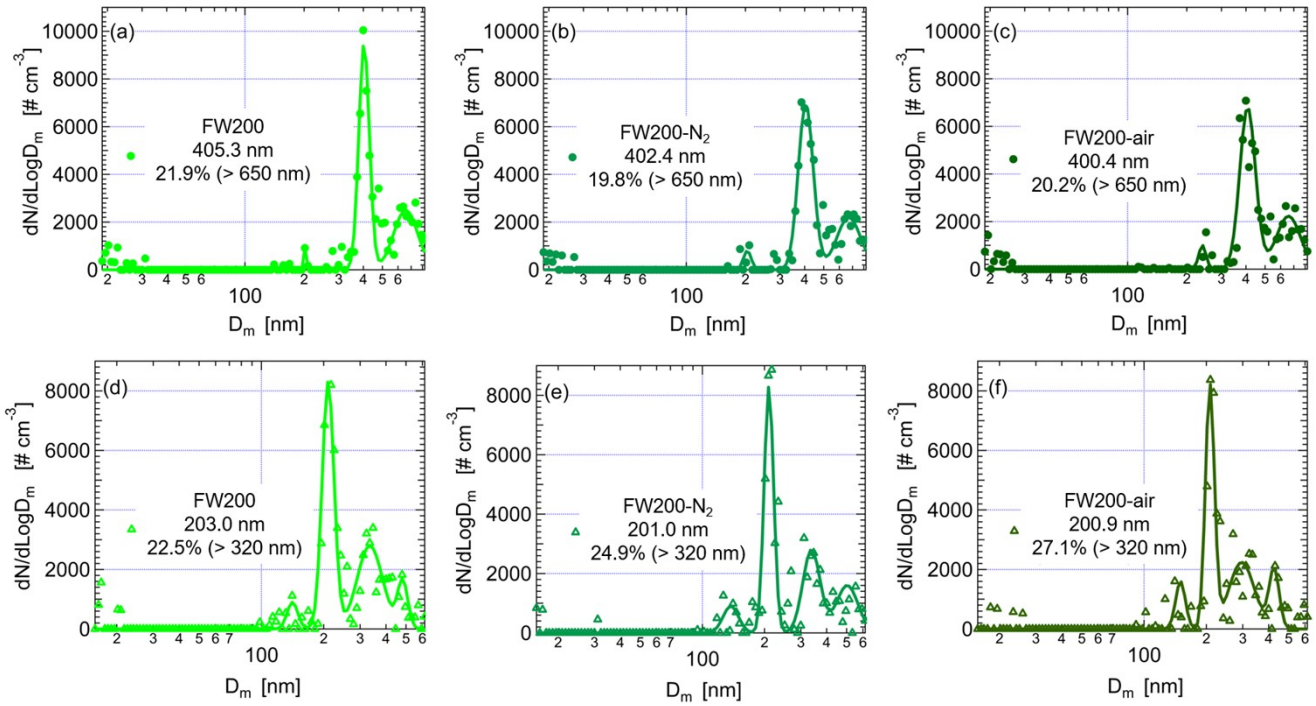

Figure S32. The size distribution of fresh and denuded 400 (a, b, c) and 200 nm (d, e, f) size-selected PR90 soot particles. Symbols and lines as in Fig. S26.

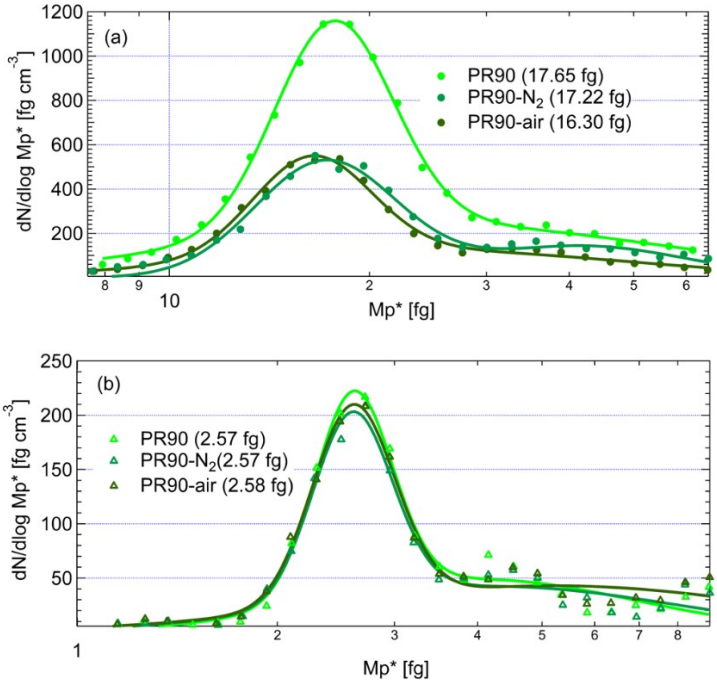

Figure S33. The mass distribution of fresh and denuded 400 (a) and 200 nm (b) size-selected PR90 soot particles. Symbols and lines as in Fig. S26.

S3 Transmission electron microscopy images of 400 nm mBlack and mBrown particles

To elucidate the thermal denuding effect on soot-aggregate morphology changes, some transmission electron microscopy (TEM) images of 400 nm mCASTblack and mCASTbrown particles were collected as shown in Fig. S34. Fresh 400 nm mCASTblack (Fig. S34a) shows a fractal aggregate with organic material coatings (see bulk shadows), which is similar to the TEM images reported for propane flame soot particles in the literature.[5,6] Compared to fresh organic-lean mCASTblack, both N_2 and air

thermal denuding do not change the particle morphology significantly as shown in Fig. S34b and c in which both mCASTblack-N_2 and mCASTblack-air particles are still fractal. This is consistent with the small mass loss (<2%) of the mCASTblack-N_2 sample at 300 °C reported by thermogravimetric analysis (TGA) measurements (Fig. 4 in the manuscript), and also the small changes in particle effective density (Fig. 6 in the manuscript) and particle mass distribution (Fig. S27a in S2) of 400 nm mCASTblack-N_2 and mCASTblack-air particles. Differently, both 400 nm mCASTbrown-N_2 and mCASTbrown-air particles (Fig. S34e and f) show a much lacier soot-aggregate structure indicting the removal of organics compared to fresh 400 nm organic-rich mCASTbrown (Fig. S34d) which presents an open-branched soot-aggregate filled with organics. The TEM results of fresh and denuded mCASTbrown samples are also in agreement with the TGA and particle density changes of the particle suggesting significant organic removal and densification of both 400 nm mCASTbrown-N_2 and mCASTbrown-air particles (see Figs. 4 and 6 in the manuscript). In summary, TEM results directly demonstrate that thermal denuding can remove some volatile material from the particle and modify the particle morphology depending on the original particle organic content. The organic removal effect may lead to porosity increase and/or active site exposure (as addressed in the manuscript Section 3.2).

The TEM images of FW200 and PR90 particles were not collected, but their soot-aggregate morphology changes induced by thermal denuding can be inferred by comparing the same auxiliary measurement results as performed for mCASTblack and mCASTbrown samples. As shown in Figs. S30 (S32) and S31a (33a) respectively, both thermal denuding conditions do not influence the particle size and mass distribution results of 400 nm FW200 (PR90), reflecting a small change in particle effective density within the measurement uncertainty and indicating insignificant changes in soot-aggregate morphology. Also, the small mass losses of FW200 and PR90 samples (<3%) at 300℃ (TGA results in Fig. 4) imply a small change in the soot-aggregate morphology after thermal denuding. Therefore, similar organic removal effect on the morphology of FW200 and PR90 particles can be deduced although the TEM measurements for FW200 and PR90 samples were not performed.

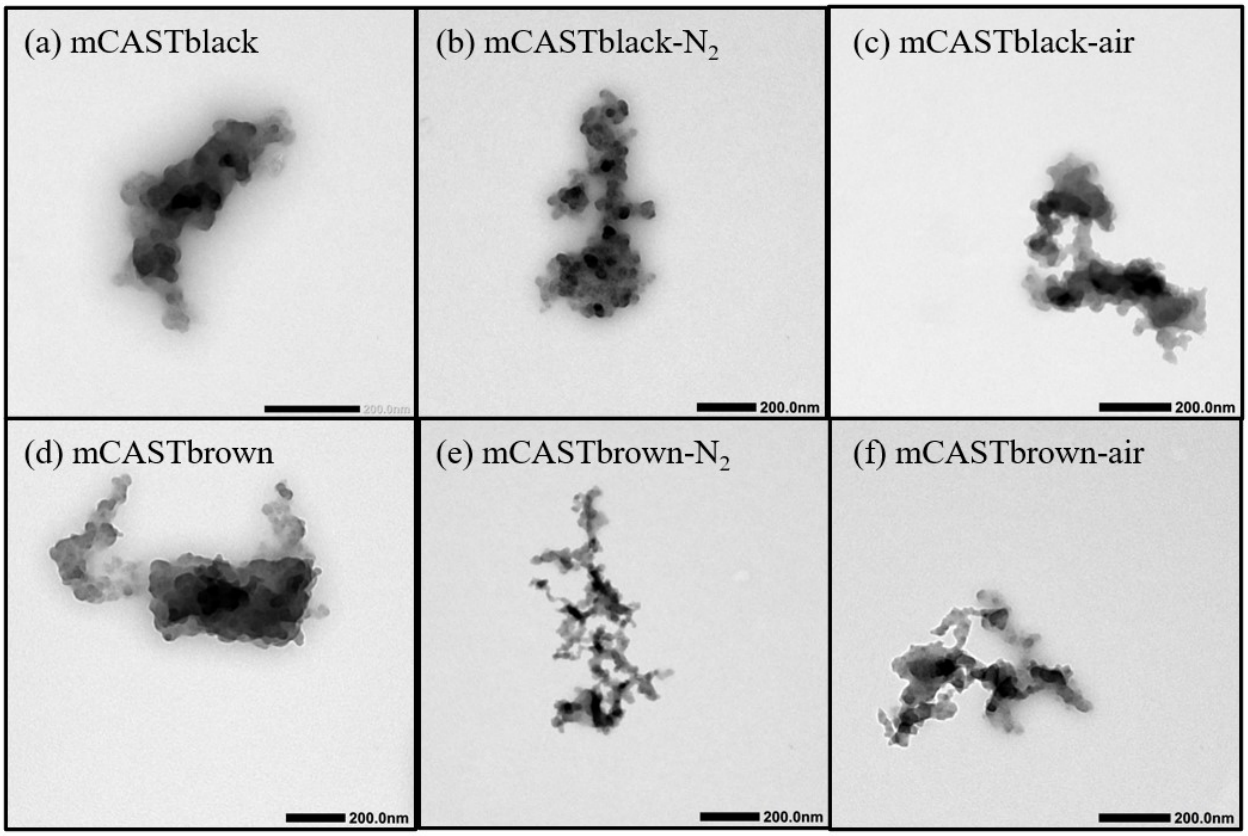

Figure S34. TEM images (microscope JEOL-1400+ TEM, JEOL Ltd., Tokyo, Japan, operated at 120 kV) for 400 nm size-selected mCASTblack and mCASTbrown particles under different thermal denuding conditions. Scale bars are indicated in each image.

References

1 T. Koop, B. Luo, A. Tsias and T. Peter, Water activity as the determinant for homogeneous ice nucleation in aqueous solutions, *Nature*, 2000, **406**, 4.

2 H. R. Pruppacher and J. D. Klett, *Microphysics of clouds and precipitation*, Kluwer, Dordrecht, 1997.

3 U. Lohmann, F. Lüönd and F. Mahrt, *An introduction to clouds from the microscale to climate*, Cambridge University Press, 2016.

4 D. M. Murphy and T. Koop, Review of the vapour pressures of ice and supercooled water for atmospheric applications, *Q. J. R. Meteorol. Soc.*, 2005, **131**, 1539-1565.

5 K. Gao, C.-W. Zhou, E. J. B. Meier and Z. A. Kanji, Laboratory studies of ice nucleation onto bare and internally mixed soot–sulfuric acid particles, *Atmos. Chem. Phys.*, 2022, **22**, 5331-5364.

6 F. Mahrt, C. Marcolli, R. O. David, P. Grönquist, E. J. Barthazy Meier, U. Lohmann and Z. A. Kanji, Ice nucleation abilities of soot particles determined with the Horizontal Ice Nucleation Chamber, *Atmos. Chem. Phys.*, 2018, **18**, 13363-13392.